ChemCatChem

ChemCatChem
Chemistry Europe
European Chemical Societies Publishing

RESEARCH ARTICLE OPEN ACCESS

Overcoming Storage Limitations in SiO_2—Supported Dual Function Materials for CO_2 Capture and Methanation

Giuseppe Nava[1] | Sergio Molina-Ramírez[2] | Matteo Di Virgilio[2] | Elisabetta Finocchio[3] | Lorenzo Viganò[2] | Barbara Di Credico[4] | Roberto Scotti[4] | Luca Lietti[1] | Cinzia Cristiani[2] | Lidia Castoldi[1]

[1]Dipartimento Di Energia, Laboratory of Catalysis and Catalytic Processes, Politecnico di Milano, Milano, Italy | [2]Dipartimento Di Chimica, Materiali e Ingegneria Chimica "Giulio Natta", Politecnico di Milano, Milano, Italy | [3]Dipartimento Di Ingegneria Civile, Chimica e Ambientale, Università di Genova, Genova, Italy | [4]Dipartimento Di Scienza dei Materiali, Università Milano-Bicocca, Milano, Italy

Correspondence: Lidia Castoldi (lidia.castoldi@polimi.it)

Received: 15 December 2025 | **Revised:** 16 February 2026 | **Accepted:** 2 March 2026

Keywords: CO_2 capture and utilization | DFM | physical mixture | ruthenium | silica | sodium

ABSTRACT

The role of the support for Dual Function Materials (DFMs) is critical in the overall activity of the materials, affecting both storage and conversion functions. Through microreactor and FT-IR investigation, the utilization of SiO_2 as support for the integrated CO_2 capture resulted in low CO_2 uptakes when using Ru- and Na- based DFMs, due to the weak protonic acidic nature of the support as well as its non-interacting nature. These properties cause the agglomeration of the Na-based sorbent, increasing its bulk basicity and lowering its effectively available amounts when higher Na loadings materials are prepared. On the other hand, higher efficiency of integrated CO_2 capture and conversion has been obtained by using segregated configurations, that is, physical mixtures of reducing/storage formulations, that in our conditions can overcome detrimental storage material-support interactions.

1 | Introduction

The increase of CO_2 levels in the atmosphere, roughly 150 ppm with respect to pre-industrialization, is strictly correlated with the worldwide temperature increase, and the scientific community is working to find effective solutions to mitigate its effects [1–3, 4].

CO_2 capture is valid alleviation method applied to point source emissions (after particulate, SO_x, and NO_x abatement), but it can be also extended to direct-air-capture (DAC) [3, 5]. Several technologies are nowadays proposed in the broad field of carbon capture [3, 6, 7], including absorption [8, 9], adsorption [10, 11], and membrane separation [12, 13]. Presently, absorption on amine-based compounds is the benchmark technology, but the high energy demand, due to the required temperature or pressure swings [3], results in high costs of the process. The separated CO_2 can either be stored in deep geological reservoirs (CCS, Carbon Capture and Storage) or used (CCU, Carbon Capture and Utilization) along with green H_2 to produce valuable synthetic chemicals and e-fuels (i.e., methane [14], methanol [15], jet fuel [16], and syngas [17]).

The production of e-methane (CH_4) is particularly appealing thanks to its easy manufacture and to the possibility to use the pre-existing distribution grid. CO_2 methanation is a catalyzed reaction called after Paul Sabatier, which follows the stoichiometry of reaction (1) [15, 18]:

$$CO_2 + 4H_2 \rightarrow CH_4 + 2H_2O \quad \Delta H_R^0 = -165\ \text{kJmol}^{-1} \qquad (1)$$

One of the drawbacks of e-methane production is related to the high separation costs of CO_2. In this respect, the reactive capture

Giuseppe Nava and Sergio Molina-Ramirez contributed equally to this work.

of CO_2, aimed at performing both capture and methanation in the same reactor, has gained attention. For this process, Dual Function Materials (DFMs) [19], where a CO_2 storage element (I or II group metals [20–23]) and a methanation metal catalyst (Ni, Ru, and Rh [24–26]) are dispersed over the same support, have been proposed. As a matter of fact, these materials are able both to capture and store CO_2 from a flue gas and convert it once green H_2 is introduced into the reactor. This enables the one-pot CO_2 abatement from point emissions followed by its conversion into methane using green H_2. Moreover, by tuning the catalysts formulations, other reactions can be carried out to valorize the captured CO_2 and convert it into different e-fuels, such as methanol [27] or syngas [28, 29]. The autothermal conduction of the cyclic methanation, that can be sustained thanks to the heat provided by the flue gas, as well as by the exothermic CO_2 adsorption and methanation reactions, represents an advantage over the traditional co-feed methanation, which needs a careful reactor design [5, 30, 31].

To date, there are still several open points on the development of DFMs, including the support effect. To the best of the authors' knowledge, mainly Al_2O_3-supported DFMs have been investigated in literature, with only few works investigating the utilization of other supports (i.e., CeO_2 [32], TiO_2 [33]). Following promising preliminary results [34], in this work SiO_2 is investigated as a support for DFMs for the integrated CO_2 capture and methanation. SiO_2 exhibits excellent textural properties, including high surface area [35], and well-defined porosity [36], which make it an attractive candidate for this application. Moreover, SiO_2 is morphologically stable even under harsh conditions, such as high temperature [37], high pressure, or in presence of steam [37]. Moreover, SiO_2 textural properties are tunable, and depending on the applied treatment, this allows to design micro-, meso- or macro-pores distribution on purpose for the final application [38]. Finally, SiO_2 could be obtained as by-product of several industrial production processes [39–41]. Therefore, the use of waste silica would simultaneously lead to a lower consumption of native natural resources and to the reduction of waste to be treated or stored in landfills, fulfilling the concepts of circular economy and sustainability.

Accordingly, in this work silica-based Ru catalysts, with different Na_2CO_3 loadings, have been prepared, characterized, and tested. The nature and the adsorption capability of the CO_2 storage sites, as well as the DFMs reactivity toward CO_2 methanation, have been assessed with microreactor experiments and FT-IR characterization. Finally, cyclic CO_2 capture and methanation experiments have been performed to study the reactivity of the material under working conditions and compared to physical mixtures of Ru/SiO_2 and Na_2CO_3/Al_2O_3. The final goal is to verify the applicability of SiO_2-supported DFMs in integrated CO_2 capture and methanation reaction.

2 | Results and Discussion

2.1 | Characterization Results

Characterization results have been carried out on the bare SiO_2 support and on the different $Ru/xNa_2CO_3/SiO_2$ active samples. As detailed in the experimental section, the active samples have been prepared by impregnation of the SiO_2 support with an aqueous solution containing Na_2CO_3; after drying and calcination at 500°C, the obtained Na_2CO_3/SiO_2 has been impregnated with an aqueous solution of Ru nitrosyl nitrate and then dried at 100°C.

Results of the textural characterization of the $Ru/xNa_2CO_3/SiO_2$ samples are reported in Figures 1A and B, while BET surface area, pores volume and pores dimensions, calculated by BJH, are summarized in Table 1. The SiO_2-supported materials present type IV isotherms, similarly to the bare support (Figure 1A); however, the textural properties of the samples are strongly influenced by the presence of Na_2CO_3. Indeed, on increasing the Na_2CO_3 loading, a progressive and marked decrease of the surface area is observed, which is already detected for the lowest Na_2CO_3 content (Table 1). This evidence is accompanied by the decrease of the pores volume (Table 1), and the increase of the average pores' width (Table 1), suggesting the blocking of the smaller pores. The progressive surface coverage is evident starting from 10% Na_2CO_3 loading, and it becomes almost complete for the $Ru/20Na_2CO_3/SiO_2$ sample. Indeed, up to Na_2CO_3 loading of 5%, the distribution of the pore dimensions is very similar to that of the bare support, evidencing only a limited displacement of the maximum of the pores average toward higher values (Figure 1B). Above 10% Na_2CO_3, the pores' distribution curves broaden with maxima at 39 and 47 nm for 10% and 15% loadings, respectively. For the highest Na_2CO_3 loading, the sample becomes almost nonporous (Figure 1B), only a flat distribution of the pores dimensions is detected, and no maximum is present. Such a behavior could be explained with a progressive pore filling with Na_2CO_3, starting from the smaller ones, thus responsible for the large surface area decrease. In particular, for the samples with a Na_2CO_3 content equal to or higher than 10 wt.%, pores with diameter lower than 10 nm are no longer detected (Figure 1B), and the average pores dimensions is the results of the contribution of the empty pores only.

XRD results of the investigated samples are shown in Figure 1C. Amorphous–microcrystalline SiO_2 (ICSD 01-076-0941) is detected in each sample, regardless of the Na_2CO_3 loading. Instead, in the $Ru/20Na_2CO_3/SiO_2$ the reflections of trona, a dihydrate sodium carbonate—sodium bicarbonate double salt ($Na_2CO_3{\cdot}NaHCO_3{\cdot}2H_2O$) (ICSD: 98-019-2711), and of sodium nitrate (ICSD: 98-001-5332) are detected. The formation of these new phases is due to the preparation method adopted for the DFMs, as they become more evident upon increasing the Na_2CO_3 loading. Indeed, the double salt is reported to form via the interaction of the Na-containing species at the surface of the impregnated samples with moisture and CO_2 of the air [42], while sodium nitrate could be related to the preparation procedure, specifically the impregnation step (without a successive calcination) with the solution of Ru precursors.

FESEM images of the different samples are shown in Figure 2. The bare SiO_2 presents a flaky surface, deriving from the crushing and sieving of 300 μm SiO_2 pellets to obtain the desired 75–106 μm granulometry. In the presence of Na_2CO_3 the overall morphology of the support is maintained; furthermore, additional agglomerates are observed. The particles with smooth surfaces (Figure 2B, F, orange arrows) are consistent with Na nitrate, and their composition is confirmed by EDX mapping

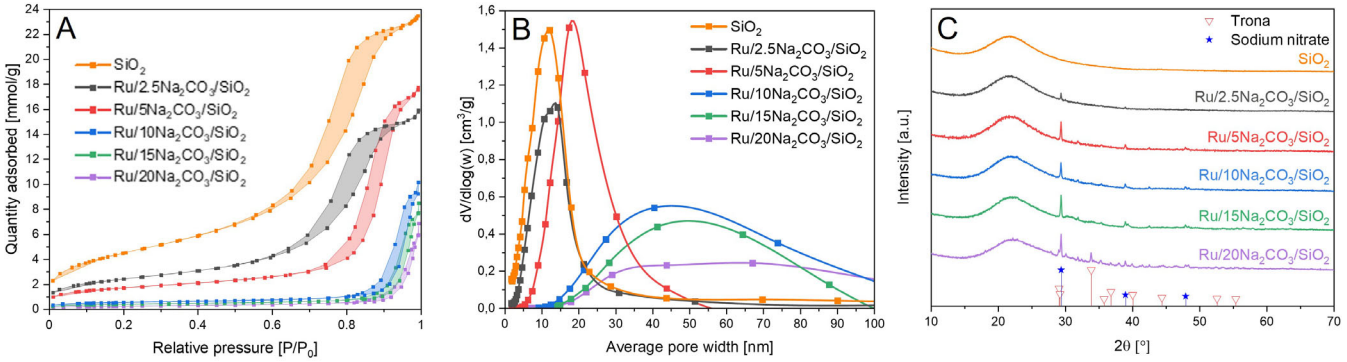

FIGURE 1 | Characterization results for SiO_2 and Ru/x Na_2CO_3/SiO_2 ($x = 2.5, 5, 10, 15, 20$): (A) N_2 adsorption–desorption isotherms, (B) Pore size distribution, and (C) X-ray diffraction patterns.

TABLE 1 | Nominal compositions and morphological characterization results.

Sample	Ru loading (wt.%)	Na_2CO_3 loading (wt.%)	BET surface area (m^2/g)	BJH Pore volume (cm^3/g)	BJH average pore width (nm)
SiO_2	0	0	360	0.83	8
Ru/2.5 Na_2CO_3/SiO_2	0.5	2.5	232	0.56	10
Ru/5 Na_2CO_3/SiO_2	0.5	5	139	0.62	18
Ru/10 Na_2CO_3/SiO_2	0.5	10	72	0.35	39
Ru/15 Na_2CO_3/SiO_2	0.5	15	33	0.29	47
Ru/20 Na_2CO_3/SiO_2	0.5	20	29	0.24	—

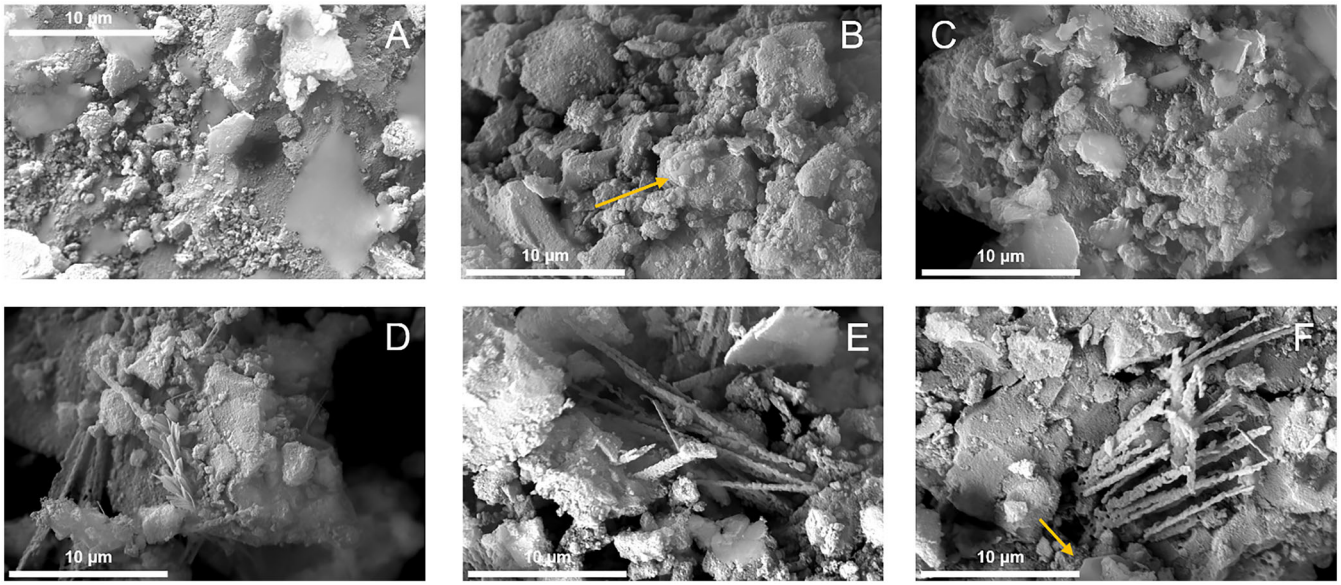

FIGURE 2 | Field emission scanning electron microscopy (FESEM) images of: (A) SiO_2; (B) Ru/2.5Na_2CO_3/SiO_2; (C) Ru/5Na_2CO_3/SiO_2; (D) Ru/10Na_2CO_3/SiO_2; (E) Ru/15Na_2CO_3/SiO_2; (F) Ru/20 Na_2CO_3/SiO_2. Orange arrows: sodium nitrate agglomerates.

(Figure S1). The sharp and elongated needles (Figure 2D–F), observed in the samples with Na_2CO_3 loadings higher than 10%, are consistent with the presence of crystalline trona [43], as confirmed by EDX mapping (see Figure S1 in Supporting Information). FESEM evidence confirms the XRD the attribution.

ATR–FTIR skeletal spectra of the sodium-based DFMs prepared with both low (5 wt.%) and high (15 wt.%) Na_2CO_3 loadings are presented in Figure 3. Characteristic signals are visible at approximately 1050 (broad), 800, and 460 cm^{-1}. These bands are assigned to the fundamental IR-active vibrational modes of silica,

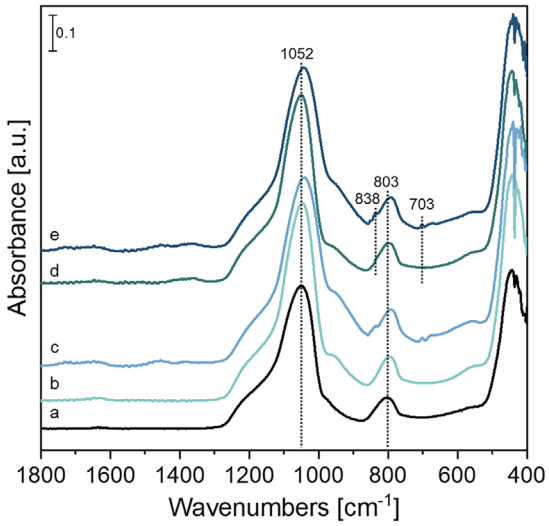

FIGURE 3 | ATR–FTIR spectra of (A) SiO_2, (B) $5Na_2CO_3/SiO_2$, (C) $15Na_2CO_3/SiO_2$, (D) $Ru/5Na_2CO_3/SiO_2$ and, (E) $Ru/15Na_2CO_3/SiO_2$.

namely the asymmetric stretching, symmetric stretching, and bending vibrations of Si—O—Si bonds within the SiO_4 tetrahedral framework [44]. These spectra appear consistently across all silica-supported materials. In addition, a marked shoulder in the 980–930 cm^{-1} region, attributed to Si—OH vibrations, is observed. This feature is known to be sensitive to surface modifications [45], and its relatively strong intensity indicates the persistence of surface silanol groups even after the incorporation of Na_2CO_3 and Ru. The preparation route and the moderate calcination temperature (500°C) likely prevent these cations from diffusing substantially into the silica bulk.

Upon introducing 15 wt.% of Na_2CO_3 (Figure 3, spectra c), additional absorption bands emerge in the 1500–600 cm^{-1} region, particularly at 838 and 703 cm^{-1}, which are characteristic of bulk carbonate species [46]. Like for other materials [47], these findings imply that surface-exposed cations are accompanied by oxide anions, favoring the in-situ generation of carbonate species via CO_2 adsorption from the ambient environment and/or because of precursor decomposition during calcination. These carbonate-related features were detected for high Na-loading samples, irrespective of Ru presence (Figure 3, spectra c and e) suggesting that low Na-content limits the formation of bulk-like Na_2CO_3 species upon calcination.

After activation in vacuum at 500°C (see Figure S2 in Supporting Information), the Ru/Na-containing samples show the typical silanol feature at 3745 cm^{-1} that decreased in intensity at increasing sodium content (commercial silica spectrum reported as comparison) [48]. This trend points to a surface perturbation induced by oxide species, which both reduces the density of accessible silanols and introduces heterogeneity among surface hydroxyl groups.

As noted earlier, bands corresponding to surface and bulk carbonate species are only evident in the sample with high sodium loading, appearing in the 1600–1300 cm^{-1} region. Their presence highlights the basic character of the modified surface and confirms that sodium-derived bulk carbonate species remain stable even after high-temperature activation under vacuum.

Reducibility of the samples has been assessed through H_2-TPR on the fresh materials, and the results are shown in Figure S3. In the case of the Ru/SiO_2 sample, the onset for H_2 consumption (due to the reduction of Ru) is observed at 125°C. The presence of Na progressively shifts to higher temperatures the onset for H_2 consumption, suggesting that Na inhibits the reducibility of Ru. Besides, in the Na-containing samples higher amounts of H_2 are also consumed, likely related to the reduction of sodium nitrates and carbonates. Over the high-loaded Na sample ($Ru/15Na_2CO_3/SiO_2$) a high-temperature reduction peak centered at 450°C is also observed, likely associated with bulk Na carbonates.

The nature of the Ru species has also been characterized through room-temperature FT-IR CO-adsorption experiments (see Figure S4 in Supporting Information), carried out on the pre-reduced Ru/SiO_2 samples containing low and high Na_2CO_3 loadings (respectively, 5 and 15 wt.%). In both cases a broad band centered at 2036 cm^{-1} was detected, accompanied by broad shoulders at higher and lower wavenumber range extending across the 2080–1950 cm^{-1} region. This feature is typically associated with bridging carbonyl species and has also been assigned by several authors to linearly coordinated carbonyls on reduced or metallic Ru particles [49]. Upon outgassing and increasing temperature, this band shifted, consistent with carbonyls adsorbed on extended metal particles whose vibrational frequency decreases at lower CO coverage due to well-known coupling effects [50, 51]. The shoulder at higher wavenumbers is assigned to characteristic carbonyl groups coordinated to partially oxidized Ru species and on Ru ions [51]. The absence of high-frequency bands above 2100 cm^{-1}, typically attributed to $Ru^{n+}(CO)_{2\text{-}4}$ species, suggests that CO did not induce Ru oxidation in the Na_2CO_3/SiO_2-based catalysts, even at high temperatures. Therefore FT-IR CO-adsorption experiments indicate that no clear differences can be pointed out by comparing the temperature evolution of the carbonyl species arising from the interaction of CO with Ru in the samples with low and high Na content.

Additional information about the different redox behavior of Ru can be assessed by performing H_2-TPR of the pre-reduced and oxidized samples. This approach allows to isolate the H_2 consumption related to the reduction of Ru oxides from that of the carbonate hydrogenation, and results are shown in Figure S5. In the case of Ru/SiO_2, the temperature onset for the reduction is observed at 125°C, like for the fresh sample. Then the H_2 consumption shows a distinct behavior with respect to the fresh sample, possibly due to some modification on Ru induced by the thermal treatment. In any case, also these experiments confirm the shift toward high temperature of the H_2 consumption in the case of the Na-containing samples, confirming the inhibition of Na on Ru reduction.

2.2 | CO_2 Adsorption–Desorption and Reaction

CO_2 Temperature Programmed Desorption (CO_2-TPD)

The interaction of CO_2 with the catalyst surface has been investigated by Temperature Programmed Desorption (CO_2-TPD) both in microreactor and in the IR cell in static conditions, to assess the stability of the stored CO_2 over the surface basic sites.

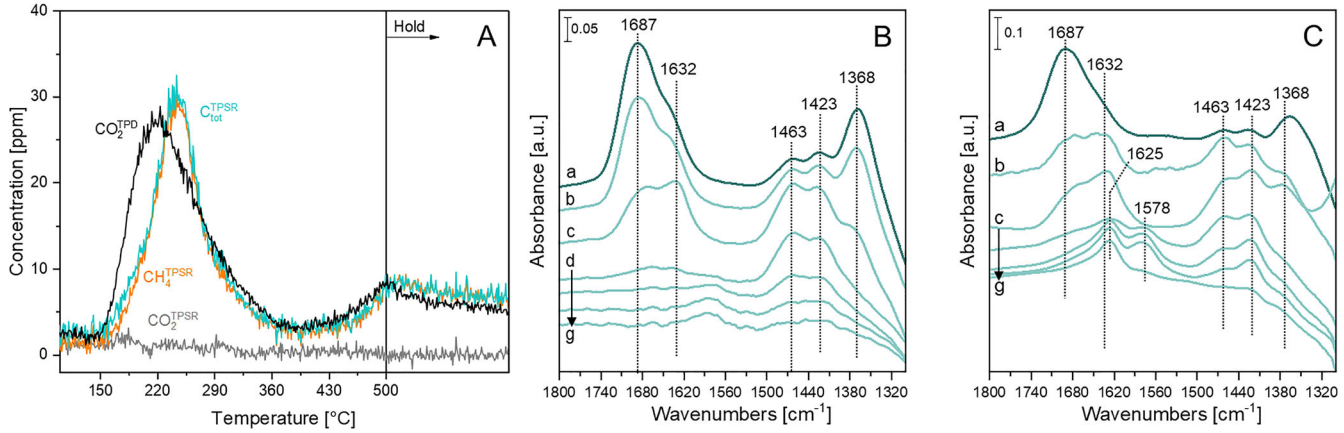

FIGURE 4 | CO_2-TPD and H_2-TPSR results for $Ru/5Na_2CO_3/SiO_2$ obtained with microreactor (panel A) and FT-IR (panel B: CO_2-TPD; panel C: H_2-TPSR) experiments. The spectrum of the activated surface was subtracted for (A) in the presence of 18 Torr CO_2 and (B) outgassing for 2 min and (C) for 1 h at R.T.; outgassing (CO_2-TPD) or in 140 Torr of H_2 (H_2-TPSR) at increasing temperature from 150°C to 300°C (step: 50°C, spectra d–g).

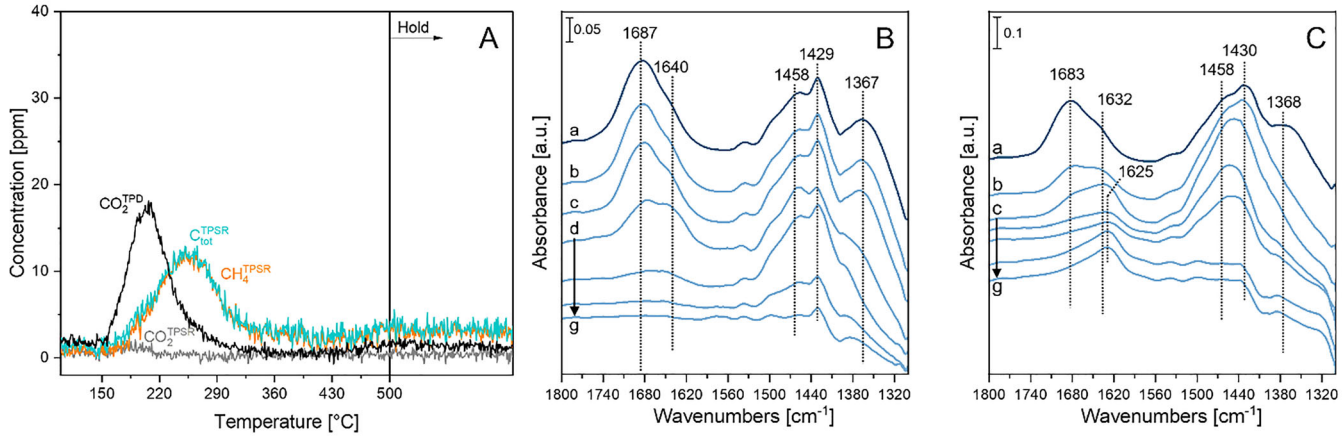

FIGURE 5 | CO_2-TPD and H_2-TPSR results for $Ru/15Na_2CO_3/SiO_2$ obtained with microreactor experiments (panel A) and FT-IR (panel B: CO_2-TPD; panel C: H_2-TPSR). The spectrum of the activated surface was subtracted for (A) in the presence of 18 Torr CO_2 and (B) outgassing for 2 min and (C) for 1 h at R.T.; outgassing (CO_2-TPD) or in 140 Torr of H_2 (H_2-TPSR) at increasing temperature from 150°C to 300°C (step: 50°C, spectra d-g).

The results of these experiments are shown in Figures 4 and 5 for $Ru/5Na_2CO_3/SiO_2$ and $Ru/15Na_2CO_3/SiO_2$, respectively, taken as examples, and in Figure S6 of the supplementary material for the other materials (only microreactor experiments). Note that the figures show the traces of CO_2 desorbed during the TPD experiments (CO_2^{TPD}), and those of CO_2, CH_4 and C_{TOT} (i.e., CO_2+ CH_4) during the H_2-TPSR experiments (CO_2^{TPSR}, CH_4^{TPSR}, and C_{TOT}^{TPSR}) that will be discussed later on. In the case of the $Ru/2.5Na_2CO_3/SiO_2$ catalyst, CO_2 desorption is observed as soon as the reactor temperature is increased and presents a single peak at 220°C (Figure S6A). No gas phase evolution of CO_2 is observed above 400°C. The quantitative analysis reported in Figure 6 shows that 21.6 $\mu molCO_2/g_{DFM}$ are stored on this sample resulting in a poor CO_2 adsorption capacity if compared with similar Na-containing catalysts supported on Al_2O_3 [20, 52], possibly associated with the prevailing weak protonic acidic nature of SiO_2 silica support.

Upon increasing the Na_2CO_3 content ($Ru/5Na_2CO_3/SiO_2$ sample, Figure 4A), an increase in the amounts of CO_2 desorbed at low temperature is observed, together with a new desorption peak at 500°C, which reaches a maximum at the end of the temperature ramp. This high temperature desorption peak is associated with strong basicity of the CO_2 adsorption sites, while the increased CO_2 desorption with respect to the previous material is consistent with the increased content of storage element in the material.

When the Na_2CO_3 content is equal to 10 wt.% ($Ru/10Na_2CO_3/SiO_2$ catalyst, Figure S6B), CO_2 is still desorbed as soon as the catalyst is heated, but the shape of the desorption peak appears narrower than in the previous cases. Moreover, a low but steady CO_2 desorption is observed during the whole temperature ramp, in the absence of a sharp high temperature peak of desorption. The reasons behind this different behavior of this sample can be ascribed to both the modified basicity of the storage element and to morphological properties of the material: the higher content of basic Na_2CO_3 leads to an increased basicity of the surface and lowers the available surface area of the material, as observed from BET results. Consequently, less storage sites are available, and those available show an increased basic nature.

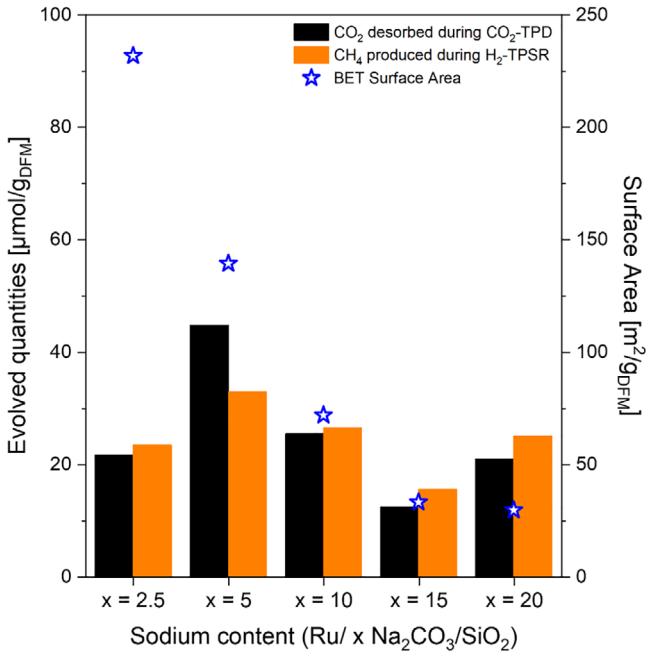

FIGURE 6 | Quantitative CO_2-TPD and H_2-TPSR results (left axis) and BET surface area (right axis) for Ru/x Na_2CO_3/SiO_2 as a function of Black columns: CO_2 desorbed during purge; orange columns: CH_4 produced during TPSR. Stars: BET surface area.

Upon further increasing of the Na_2CO_3 content (Ru/15Na_2CO_3/SiO_2 sample, Figure 5A), the low temperature CO_2 desorption peak is furthermore decreased, and in general the amount of desorbed CO_2 is lower than every sample previously reported.

Finally, in the Ru/20Na_2CO_3/SiO_2 sample (Figure S6C) the low temperature peak is even weaker, while at higher temperatures some CO_2 desorption is observed.

TPD experiments results highlight the poor CO_2 capacity of SiO_2-supported DFMs even when the content of Na_2CO_3 is high. Comparing the amounts of desorbed CO_2 (Figure 6, black columns), in the best case (Ru/5Na_2CO_3/SiO_2: 42 μmol/g_{DFM}) the uptake is one order of magnitude lower with respect to typical Al_2O_3-supported DFMs reported in literature [20, 52], pointing out that the role of the support for the CO_2 storage capacity is crucial. The low interactive nature of SiO_2, that has been reported with respect to Ru/SiO_2 methanation catalysts [36], could also play a role for the dispersion of the Na_2CO_3: at low loadings Na appears to be homogeneously dispersed, while at higher loadings the loss in surface area and the increased basicity of the CO_2 adsorption sites suggest that larger Na-containing particles are formed, thus introducing increased contents of bulk carbonates species with high thermal stability [53].

The nature and thermal stability of the surface species formed upon CO_2 adsorption were investigated with FT-IR spectroscopy for the samples with 5 and 15 wt.% Na_2CO_3 loadings, and results are shown in Figures 4B and 5B, respectively. Before adsorption, the samples were activated under vacuum and subsequently saturated with CO_2 at room temperature to ensure maximum surface coverage. The samples were then subjected to stepwise outgassing between 150°C and 300°C, with temperature increments of 50°C.

The CO_2 adsorption–desorption FT-IR experiments performed on samples with low and high Na loadings reveal the formation of a complex array of carbonate-related surface species within the 1800–1320 cm^{-1} region. For the low Na-loading sample, Ru/5Na_2CO_3/SiO_2 (Figure 4B), distinct bands were observed at 1687 cm^{-1} (ν_{3as}) + 1368 cm^{-1} (ν_{3s}) and 1632 cm^{-1} (ν_{3as}), corresponding to O—C—O stretching vibrations. These features are associated with two different bidentate carbonate species [54] formed upon CO_2 exposure at room temperature. Both bands disappeared upon outgassing at 150°C, indicating their relatively low thermal stability as observed previously at CO_2-TPD microreactor test. Additional bands centered at 1463 and 1423 cm^{-1} were detected and assigned to polydentate carbonate species [46, 54]; and strongly bonded bidentate chelating carbonates [55–57] formed on Na oxide, respectively. The 1463 cm^{-1} band persisted upon heating up to 250°C, whereas the 1423 cm^{-1} band remained visible up to 300°C. This effect indicates that these carbonate species are not desorbed until the medium-to-high temperature range, highlighting their enhanced thermal stability compared to the bidentate species formed at room temperature. Similar results were also reported by Keturakis et al. [54] and Proaño et al. [58] for sodium-based materials supported over alumina.

A similar population and evolution of carbonate species were observed during the CO_2-TPD FT-IR test for the sample with a higher Na_2CO_3 loading (15 wt.%), e.g., Ru/15Na_2CO_3/SiO_2 (Figure 5B). As in the low-loading sample, bands associated with bidentate carbonate species were detected at 1387 and 1367 cm^{-1}, along with a signal at 1640 cm^{-1}. These features progressively decreased in intensity and disappeared upon outgassing at 150°C, indicating their limited thermal stability. In contrast, the bands at 1458 and 1429 cm^{-1}, corresponding to thermally more stable polydentate and bidentate chelating carbonate species, exhibited higher relative intensities compared to the low Na-loading sample. This suggests that increasing the Na content promotes the formation of more strongly bonded carbonate species, requiring evacuation temperatures of approximately 300°C for polydentate carbonates and above 350°C for bidentate chelating species to achieve complete desorption.

As expected, the substantial increase in sodium loading, while keeping the Ru phase concentration constant, enhanced the CO_2 retention capacity of the silica-supported materials as was reported in literature [20, 59, 60], however, as observed in CO_2-TPD microreactor tests, the increase of Na loading exceeding 10 wt.% over SiO_2 led to a reduction of the overall CO_2 retention capacity, likely due to the presence of larger Na_2CO_3 particles that provokes a decreasing of the specific surface area, resulting in reduced availability of the active storage sites. Although the chemical nature of the adsorbed species remained similar, the overall carbonate population shifted toward carbonate species with higher thermal stability. Similar trends were reported by Keturakis et al. [54] for CO_2 adsorption-desorption experiments performed on alumina-supported samples with varying Na_2O loadings.

H_2 Temperature Programmed Surface Reduction (H_2-TPSR)

Temperature Programmed Surface Reduction with H_2 (H_2-TPSR) experiments have been performed to study the reactivity of the surface carbonates in presence of H_2. Results of H_2-TPSR experiments are shown in Figure 4 for $Ru/5Na_2CO_3/SiO_2$, Figure 5 for $Ru/15Na_2CO_3/SiO_2$, and in Figure S6 of the supplementary material for the other materials. Quantitative results are reported in Figure 6.

After saturation with CO_2, $Ru/2.5Na_2CO_3/SiO_2$ is exposed to H_2 (4% H_2/He v/v) and heated to 500°C (heating rate: 10°C/min). As soon as the temperature is increased, the signal of CH_4 starts to increase reaching a maximum at 280°C. After this temperature, the concentration rapidly decreases until approaching zero by the temperature of 400°C. Comparing the evolution of gas phase species during the TPD and TPSR experiments, it is observed that the peak of CO_2 desorption during TPD (i.e., CO_2^{TPD}) is detected at lower temperatures with respect to the evolution of the carbonaceous species (mainly CH_4) during the TPSR run. It is suggested that during the TPSR run, at low temperatures CO_2 is converted to CO, that remains adsorbed on reduced Ru sites as a Ru-carbonyl [61] and this explains the observed delay in the evolution of C-species in the TPSR run with respect to the TPD experiment. Although CO is not observed in the microreactor experiments, FT-IR studies of carbonate hydrogenation in static conditions evidenced very weak features at 2042 cm^{-1} and in the range 2000–1950 cm^{-1}, associated with bridging carbonyl species over Ru particles [50, 62] (see Figure S7 in Supporting Information).

Similar conclusions can be drawn for $Ru/5Na_2CO_3/SiO_2$, where only a small shift to higher temperatures for the onset of methane formation is observed with respect to CO_2 evolution during the TPD experiment.

At variance, for $Ru/10Na_2CO_3/SiO_2$, a CO_2 desorption peak is observed before the CH_4 production peak during TPSR, indicating that Ru starts to be active toward CO_2 activation at slightly higher temperatures. Moreover, the temperature difference between the peak of CO_2 desorption during TPD and CH_4 formation in TPSR appears to be greater with respect to the previous samples. Along similar lines, in the $Ru/15Na_2CO_3/SiO_2$ and $Ru/20Na_2CO_3/SiO_2$ samples having the highest Na content, methane formation is further delayed, and this is particularly evident for the latter sample: CH_4 starts to be produced only above 200°C, with a peak at 500°C.

These data indicates that at low Na_2CO_3 loadings, the high surface area of the silica support ensures an appreciable dispersion of the alkali component. As the Na_2CO_3 loading increases, a higher amount of sodium agglomerates forms, which consequently reduces the number of accessible CO_2 storage active sites. Besides, an inhibition effect is observed of the alkali component on the methanation reactivity.

The reduction of the adsorbed CO_2 was further examined by in situ FT-IR spectroscopy for the $Ru/5Na_2CO_3/SiO_2$ (Figure 4C) and $Ru/15Na_2CO_3/SiO_2$ (Figure 5C) samples. In this set of experiments, after saturation with CO_2 at room temperature to ensure maximum coverage of the surface, the sample was first subjected to prolonged outgassing at room temperature, followed by a stepwise temperature ramp from 150°C to 300°C under H_2 atmosphere.

As for the lowest Na concentration (Figure 4C), the main bands of the spectra are due to carbonate species, whose intensities evolve upon exposure to hydrogen. No additional features associated with formate species typically observed during CO_2 methanation over Ru/Al_2O_3 or Na-based dual-function materials [58, 63–65], could be clearly identified. In agreement with the microreactor analysis (Figure 4A), a rapid and marked decrease in carbonate band intensity was observed as the temperature increased under hydrogen, indicating the progressive reduction of these species.

The peak at 1625 cm^{-1} was detected starting at 200°C and is attributed to the presence of molecularly adsorbed water on the surface [66]. The appearance of water as a reaction product is linked to the reduction of carbonate species to methane (see gas-phase signal in Figure S8A) through the methanation process, as confirmed by microreactor tests. As observed, the thermally stable carbonate species, namely polydentate carbonates (1463 cm^{-1}) and strongly bonded bidentate chelating carbonates (1423 cm^{-1}), were not perturbed until 200°C. Instead, a sequential reduction occurs: the band at 1463 cm^{-1} decreases first and completely disappears at 250°C, followed by the progressive reduction of the 1423 cm^{-1} band. This latter reduction occurs concurrently with the emergence of a new band at 1578 cm^{-1}, assigned to bidentate bridged carbonates [46], which are fully reduced to methane at 300°C. This phenomenon suggests that bidentate chelating carbonates are converted to methane through two parallel pathways: (i) direct carbonate reduction at isolated Na sites, and (ii) conversion to thermally stable bridging bidentate carbonates (at neighboring Na sites), which are subsequently reduced to methane at higher temperatures.

An increase in the Na_2CO_3 loading of the catalyst led to a similar overall evolution of surface species (Figure 5C), albeit with some differences in their behavior upon heating in hydrogen atmosphere after CO_2 capture phase. As revealed by the analysis of gas phase species in the IR cell, the presence of more thermally stable carbonates on the catalyst surface following CO_2 capture resulted in a shift of their reduction to CH_4 toward higher temperatures. In the gas phase (Figure S8B), methane formation was not detected below 250°C, indicating that polydentate (~1460 cm^{-1}) and bidentate chelating (~1430 cm^{-1}) carbonates exhibit greater thermal resistance in the presence of hydrogen. The excess Na_2CO_3 loading in the silica-supported dual-function materials possibly promotes a high dispersion of Ru species on the surface, which ultimately reduces the surface regeneration capacity through the H_2 spillover mechanism.

To summarize, the amounts of CO_2 desorbed during CO_2-TPD runs and the C-containing species (CO_2, CH_4) evolved during H_2-TPSR experiments are shown in Figure 6, along with their respective BET surface area value. The amounts of desorbed species per gram of catalyst appears to present a maximum for $Ru/5Na_2CO_3/SiO_2$, indicating that no beneficial effect is obtained by further increases of the Na_2CO_3 contents. As already discussed for CO_2-TPD, the increases of Na_2CO_3 loading are not accompanied by a correspondent increase of the CO_2 storage

capacity due to agglomeration of the alkali component, and thus of the CH_4 production. Similar results were reported by Bahrami et al. [67]. They revealed that the increase of Na-loading for Ru-Na based DFMs supported on CeO_2-Al_2O_3 did not result in a linear increase of CO_2-uptake capacity along with CH_4-production during H_2-TPSR. This can be due to the increase in the loading of Na-containing species which leads to differences in the formation of Na oxide due to the precursor reducibility because of Na-agglomeration on the support. Moreover, while medium basic sites increase by increasing the loading of the absorbent, the catalytic material should also be sufficiently available with a higher surface area to convert this adsorbed CO_2.

2.3 | Reactivity During CO_2–H_2 Co-Feed

CO_2–H_2 co-feed experiments have been performed to determine the activity of the catalyst toward the methanation of CO_2. Experiments have been performed by feeding CO_2 and H_2 in stoichiometric amounts (ratio 1:4) while increasing the temperature to 400°C, and the results are shown in Figure S9 of the supplementary material.

As for Ru/SiO_2 catalyst (Figure S9A), which has been used as reference, it is possible to observe that CO_2 is converted starting from 125°C. From this temperature onward, CH_4 is initially produced, followed by CO production. Upon increasing the temperature, CO selectivity increases at the expense of CH_4, coherently with thermodynamic constraints [68]. Once 400°C are reached, CO_2 conversion reaches a plateau while the selectivity toward CO and CH_4 slightly change over time, progressively favoring CO production.

The doping of the SiO_2 support with small amounts of Na_2CO_3 (Figure S9B: 2.5 wt.% and Figure S9C: 5 wt.%) leads to a change in selectivity of the DFM: once CO_2 is starting to be converted, CO is the first observed reduction product. After a small delay, CH_4 starts to be produced, and its selectivity steadily increases until the reaching of 400°C. Although less methane is produced with respect to the Ru/SiO_2 case, CH_4 selectivity is greater than 20% for both $Ru/2.5Na_2CO_3/SiO_2$ and $Ru/5Na_2CO_3/SiO_2$, indicating a mild inhibition of the methanation reaction in the presence of Na.

Notably, a lower CH_4 selectivity is observed during the CO_2–H_2 co-feed experiments if compared to the H_2-TPSR runs. This is likely related to the different H_2–CO_2 ratios that is attained on the catalyst surface during these two sets of experiments. In fact, during H_2-TPSR, a feed of H_2 is sent to the carbonated sample and under these conditions we expect a very high H_2–CO_2 ratio on the surface in view of the slow CO_2 release/desorption from the surface. At variance, when performing CO_2 and H_2 co-feeding experiments, the H_2–CO_2 ratio on the surface is significantly lower since CO_2 is continuously fed, and under these conditions an increase in the CO selectivity is observed at the expenses of CH_4.

For further increases of the amounts of Na_2CO_3 (Figure S9D: 10 wt.%, Figure S9E: 15 wt.%, and Figure S9F: 20 wt.%), CH_4 selectivity is further inhibited, with values always below 10%. CO is the main product of CO_2 reduction, pointing out that the inhibition of the alkali component on the methanation reaction.

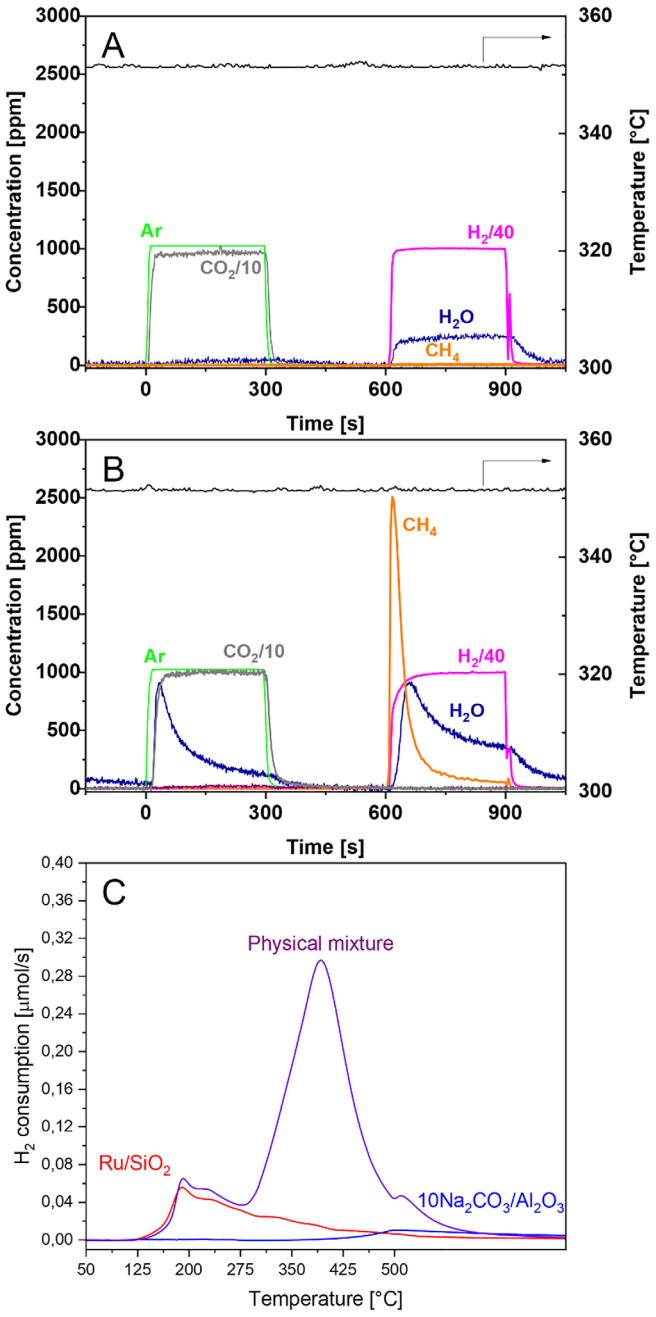

FIGURE 7 | Panels A, B: Results of isothermal cycles performed under model conditions at 350°C (adsorption: 1% CO_2/He, 5 min; reduction: 4% H_2/He, 5 min) for $Ru/10Na_2CO_3/SiO_2$ sample (panel A) and for the physical mixture of Ru/SiO_2 and $10Na_2CO_3/Al_2O_3$ and (panel B); panel C: results of H_2-TPR experiments for Ru/SiO_2 (red line), $10Na_2CO_3/Al_2O_3$ (blue line) and their physical mixture (purple line). After reaching 500°C, temperature was kept constant.

2.4 | Isothermal CO_2 Capture and Methanation Cycles

The application of SiO_2-supported DFMs for the cyclic capture and methanation of CO_2 has been investigated through alternating cyclic experiments, and the resulting cycles in model conditions (i.e., only CO_2 during the adsorption phase) are reported in Figure 7.

When exposing $Ru/10Na_2CO_3/SiO_2$ (Figure 7A) to a CO_2 containing atmosphere (i.e., $t = 0$ s), the signal of the CO_2 and the signal of the tracer (Ar) are detected at the same time, indicating the absence of a breakthrough time. Then, the CO_2 signal is evolving slower than the evolution of the tracer, indicating that some degree of CO_2 adsorption is taking place. When CO_2 is removed to start the purge phase (i.e., $t = 300$ s), the majority of the just stored CO_2 is desorbed, indicating a low stability of the adsorbed species, leading to negligible CH_4 yields during the successive reduction phase ($t = 600$–900 s).

Confirming what reported in the previous paragraphs, Ru/Na formulations evidenced limited CO_2 capture capacity when supported over SiO_2. On the other hand, Ru/SiO_2 itself shows activity in CO_2 methanation [69–71], suggesting the utilization of an alternative approach: separating the adsorption functionality from the methanation one, possibly by using different supports for each component. In this sense, we tested a physical mixture of a methanation catalyst (i.e., Ru/SiO_2) and a CO_2 sorbent (i.e., Na_2CO_3/Al_2O_3, 10 wt.%) to overcome the limitations concerning the CO_2 storage capacity of the SiO_2-based systems [52]. Cycles of CO_2 adsorption and methanation have been performed (Figure 7B) and compared with the ternary configuration of $Ru/10Na_2CO_3/SiO_2$ previously discussed. Note that equivalent amounts of Ru and Na_2CO_3 are present in the two catalytic systems, differing only for their relative support.

The results of model cycles for the mechanical mixture of Ru/SiO_2 and Na_2CO_3/Al_2O_3 (Figure 7B) show that after CO_2 admission to the reactor, a dead time is observed before it is detected in the gas phase, indicating complete CO_2 adsorption. After the breakthrough time, CO_2 is rapidly evolving in the gas phase until reaching its steady state value, indicating the saturation of the catalyst. After CO_2 switch-off (i.e., at 300 s), during the purge in He, CO_2 concentration decreases, indicating partial desorption of the stored CO_2. Finally, when H_2 is fed ($t = 900$ s) a sharp evolution of the CH_4 peak is observed, along with a consumption of H_2, indicating that the methanation of the previously stored CO_2 is taking place. In this condition the catalyst is able to produce 71 $\mu mol/g_{PM}$ of CH_4 with complete selectivity.

Noticeably, a delay with respect to CH_4 evolution, a peak of H_2O is also detected, likely associated to the desorption of H_2O produced from the methanation and previously adsorbed (in agreement with IR data in the previous paragraphs). By comparing the results of the ternary catalyst with the mechanical mixture, the advantage of using the latter is evident.

Similar behavior is observed when testing the catalysts under simulated flue gas conditions, that is, in the presence of CO_2, O_2 and H_2O (Figure S10): $Ru/10Na_2CO_3/SiO_2$ still captures low CO_2 amounts and consequently produces negligible CH_4 quantities (Figure S10A). On the other hand, the physical mixture (Figure S10A) captures a lower amount of CO_2 with respect to the model case (i.e., only CO_2 during adsorption phase) due to the competitive adsorption mechanism between CO_2 and H_2O for the same Na adsorption sites, translating to a lower CH_4 production (37 $\mu mol/g_{PM}$) during the reduction phase. Apparently, since the methane peak does not appear with a delay with respect to the injection of H_2, the presence of O_2 seems to not induce any modification of the Ru activity during the reduction phase, indicating a good reducibility of Ru.

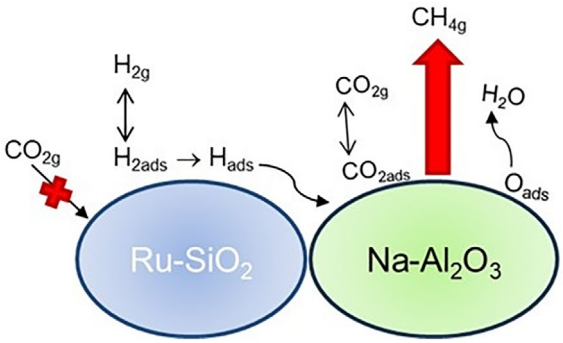

FIGURE 8 | Scheme of methanation reaction on Ru/SiO_2–Na/Al_2O_3 physical mixture.

The results of these experiments point out that physical mixtures are able to effectively produce CH_4 during cyclic operations. The obtained CH_4 yield is similar to the ones reported in the literature in the same conditions with other physical mixtures formulations (Table S1), indicating the effectiveness of this configuration. The mechanisms behind the activity of the physical mixture are still under discussion and could be related to thermal effects [74] due to the exothermicity of CO_2 methanation, leading to CO_2 desorption and methanation, and/or to the spillover of activated hydrogen from Ru to the sorbent [75]. In contrast with traditional DFMs, where superficial intra-particle spillover has been recognized to enhance the catalytic activity [72, 73], in the case of physical mixtures the spillover should be inter-particle [76] due to the segregation of the methanation and storage functions. Likely, in this case the inter-particle H-spillover occurs when H_2 is activated on Ru/SiO_2 and is then transported to Na_2CO_3/Al_2O_3 particles to allow the CO_2 reduction, as depicted in the Figure 8. This mechanism is supported by H_2-TPR experiments performed over Ru/SiO_2, Na_2CO_3/Al_2O_3 and Ru/SiO_2-Na_2CO_3/Al_2O_3 physical mixture (Figure 7C). The H_2 consumption measured for the physical mixture (243 μmol) is significantly higher than that of the Ru/SiO_2 and Na_2CO_3/Al_2O_3 samples (52 and 14 μmol, respectively). This indicates that in the physical mixtures H_2 activated over Ru is able to spill to Na_2CO_3/Al_2O_3 where it is consumed in the reduction of the carbonates, as sketched in Figure 8.

The presence of the interparticle spillover in the physical mixture allows to overcome the limitations given by unwanted interactions between the hydrogenation metal and the storage element, when dispersed over the same support. Once the H_2 transfer is guaranteed from the hydrogenation metal to the adsorbed CO_2, the optimization of the individual reactivity of the methanation and storage functions is also possible.

3 | Conclusions

In this work, the utilization of SiO_2 supported DFMs for the integrated capture and methanation of CO_2 has been investigated. The interactions between SiO_2 and Na lead to limited CO_2 uptakes, which do not change even when increasing the amounts

of Na in the material. The reasons behind this inhibition rely on the drastic reduction of the surface area of the materials following Na doping, as well as due weak protonic acidic nature of SiO_2. Moreover, FT-IR spectroscopic investigation evidenced the high stability of carbonate species formed following CO_2 adsorption that limits CO_2 desorption ability even at high temperatures. On the other side, physical mixtures of Ru/SiO_2 and Na_2CO_3/Al_2O_3 have been used under cyclic CO_2 capture and reduction conditions, leading to interestingly good results if compared to the ternary Ru/Na/Silica formulations. This is related to the presence of H_2-interparticle spillover that guarantees the H_2 transfer from the hydrogenation metal to the adsorbed CO_2, opening the way toward the optimization of the individual reactivity of the methanation and storage functions.

4 | Experimental Section

4.1 | Catalyst Preparation

Commercial SiO_2 (BASF, crushed and sieved to 75–106 μm particles) was used as support to prepare different catalysts, whereas commercial γ-Al_2O_3 (Sasol Puralox, 75–106 μm) was employed to prepare a reference sample.

The Si-based catalysts were prepared via incipient wetness impregnation method [52]. The supports were impregnated with Na_2CO_3 aqueous solutions (final loading 2.5–20 wt.% Na_2CO_3), dried at 110°C for 12 h, and calcined at 500°C for 5 h (heating rate 2°C/min). The obtained samples were then impregnated with an aqueous solution of Ru nitrosyl nitrate ($Ru(NO)(NO_3)_x(OH)_y$, $x + y = 3$, Alfa Aesar, 15.5 mg_{Ru}/mL) to obtain a final loading 0.5 wt.% Ru, and then dried at 110°C for 12 h; these dried samples were thus characterized and tested. The prepared samples $Ru/xNa_2CO_3/SiO_2$, where x is the Na_2CO_3 weight percentage, are identified in the text with acronyms indicating the composition and the Na content; for example, $Ru/2.5Na_2CO_3/SiO_2$ identifies the sample containing 2.5 wt.% of Na_2CO_3. Using the same procedure, a Ru/SiO_2 sample, nominal Ru loading equal to 0.5 wt.%, was also prepared and subjected to the same drying treatment (100°C, 12 h).

The reference Al-based sample (Na_2CO_3/Al_2O_3, hereafter) was obtained by impregnation of the support to reach a nominal Na_2CO_3 loading of 10 wt.%. The sample was dried at 110°C for 12 h and calcined at 500°C for 5 h (heating rate: 2°C/min).

Finally, a physical mixture of Ru/SiO_2 and Na_2CO_3/Al_2O_3 was obtained by thoroughly mixing the same weighted amount of both samples.

4.2 | Catalyst Characterization

Specific surface area and pore volume of the prepared samples were measured by adsorption-desorption of nitrogen (N_2) at -196°C using a Micrometrics Tristar 300 instrument. Prior to the measurement, the samples were outgassed under vacuum at 120°C for 3 h. Brunauer–Emmett–Teller (BET) surface area and pore volume were determined by the Barrett–Joyner–Halenda (BJH) method, using the adsorption branch of the isotherm.

X-ray diffraction (XRD) patterns were collected using a Panalytical diffractometer (Empyrean model) in Bragg–Brentano geometry fitted with a copper tube (Cu Kα radiation). The data sets were acquired in continuous scanning mode over the 2θ range 5°–70°, using a step interval of 0.0260° and step time of 110 s. Inorganic Crystalline Structure Database (ICSD) has been used to identify the crystalline phases.

Sample morphology and the distribution of the active elements were assessed by a Field Emission Scanning Electron Microscope (FESEM, Zeiss Sigma 500) equipped with an energy dispersive X-ray detector (EDX, Oxford Ultimax 65).

Skeletal Fourier-transform infrared (FT-IR) spectra of catalyst powders were recorded in a FT-Instrument (ThermoNicolet) equipped with an ATR accessory (diamond window), collecting 100 scans with a resolution of 4 cm^{-1} and background air (DTGS detector and OMNIC software).

Adsorption and desorption of probe molecules FT-IR experiments were carried out in transmission mode over pure powder disks (25 mg average disks weight) directly in an IR cell connected to a conventional gas manipulation apparatus. Before each adsorption experiment, samples were activated in vacuum (10^{-3} Torr) for 1 h at 500°C or reduced at the same temperature in hydrogen and subsequently outgassed at 500°C. CO adsorption and desorption tests were carried out over the pre-reduced samples (400 Torr of H_2 during 1 h at 500°C and subsequent outgassing for 1 h) at R.T., and spectra were recorded upon outgassing and warming in the temperature range from R.T. up to 300°C (50°C/step).

Reducibility of the materials has been assessed through H_2-TPR experiments, carried out using a TPDRO 1100 instrument (ThermoFisher) by feeding 5% H_2/Ar and heating from room temperature to 500°C (heating rate: 10°C/min). Reducibility of Ru has been assessed by repeating H_2-TPR experiments after sequential H_2-TPR (to remove carbonates) and temperature programmed oxidation (TPO), performed by feeding 2% O_2/Ar and heating from room temperature to 500°C (heating rate: 10°C/min).

4.3 | In-Flow Characterization and Testing Experiments

Catalytic in-flow characterization and testing were performed through microreactor and FT-IR setups. Microreactor experiments have been carried out by loading 60 mg of catalyst in a quartz microreactor (internal diameter 8 mm). The catalytic bed has been packed in the reactor using quartz wool and the rest of the reactor volume has been filled with quartz granules to reduce the void volume, ensuring a proper mixing of the feed gases. Temperature has been monitored using a K-type thermocouple placed in the center of the catalytic bed.

Every microreactor experiment has been performed using a constant gas flow rate of 100 mL(STP)/min, corresponding to 100 L(STP)/h/g_{cat}. Gases have been dosed using Brooks mass flow controllers and sent to two 4-way-valves, allowing to stepwise change the feed composition when switching the position of the valve. In this direction, in each valve two identical gas

flow rates are fed, consisting in a reagent (i.e., CO_2 or H_2) and an equal flow rate of He, which has also been used as carrier gas, allowing to change the gas phase composition without affecting the total gas flow rate. The composition of the gases at the outlet of the reactor have been monitored using a Mass Spectrometer (Pfeiffer Vacuum, analysis every 4 s) and a micro-gas Chromatograph (Agilent, analysis every 180 s) equipped with two different chromatographic columns.

Each catalyst has been pre-treated in H_2 atmosphere (4% H_2/He v/v) at high temperature (500°C, heating rate: 10°C/min) to decompose the precursor of Ru and reduce it to its metallic form. The same pretreatment has been repeated before each experiment, to remove any adsorbed species that could have been adsorbed from air (i.e., CO_2, H_2O).

The stability and reactivity of the adsorbed CO_2 have been gathered respectively from Temperature Programmed Desorption of CO_2 (CO_2-TPD) and Temperature Programmed Surface Reduction with H_2 (H_2-TPSR) experiments, respectively. After CO_2 saturation at 150°C, the catalyst was heated to 500°C (heating rate: 10°C/min) in inert atmosphere (He) to perform CO_2-TPD or reducing atmosphere (4% H_2/He v/v) to perform H_2-TPSR.

Similarly, CO_2-TPD experiments were performed in the FT-IR setup by introducing into the IR cell 18 Torr of pure CO_2 at room temperature and then outgassing at R.T. for 1 h. Subsequently, spectra of the surface species were recorded at each desorption T-step in the range 150–300°C. Differently, to perform H_2-TPSR after CO_2 adsorption phase and outgassing at room temperature, 140 Torr of pure H_2 were introduced in the IR cell at room temperature, and then spectra of the surface species and gas phase were recorded at each temperature in the range 150–300°C maintaining H_2-atmosphere.

Reactivity under stoichiometric amounts of CO_2 and H_2 (CO_2:H_2 = 1:4) for the Sabatier reaction was investigated in the microreactor setup by co-feeding CO_2 and H_2 (1% CO_2 + 4% H_2 v/v in He) while increasing the temperature up to 400°C (heating rate: 10°C/min). After 30 min, the temperature was decreased (heating rate: −10°C/min) still in presence of CO_2 and H_2 until R.T. was reached.

Reactivity under adsorption and reduction isothermal cycles has been performed at 350°C in microreactors. Cycles are performed by alternating an adsorption phase (5 min, 1% CO_2/He v/v) and a reduction phase (5 min, 4% H_2/He v/v) spaced out by a purge in inert (5 min, He). Three cycles were performed for each experiment to obtain reproducible results. To conclude the experiment, the catalyst is heated to 500°C (heating rate: 10°C/min) in H_2 (4% H_2/He) to desorb eventual unreacted adsorbed species. Cyclic experiments have been performed in model conditions (adsorption phase: 1% CO_2/He v/v) or in simulated flue gas conditions (adsorption phase: 1% CO_2 + 3% O_2 + 2% H_2O in He v/v) to observe the influence of such conditions on the reactivity. For the physical mixture, equivalent amounts of active phases (i.e., Ru and Na_2CO_3) have been used, thus loading twice the amount of catalyst (i.e., 60 mg Ru/SiO_2 + 60 mg $10Na_2CO_3/Al_2O_3$). A different quartz microreactor has been used (internal diameter 11 mm) to maintain the same height of the catalytic bed. For the quantitative calculations, moles of evolving species (i.e., CO_2, CH_4) have been divided by 60 mg for DFMs (i.e., $\mu mol/g_{DFM}$) and 120 mg for physical mixtures (i.e., $\mu mol/g_{PM}$).

Acknowledgments

The authors acknowledges the financial support of Piano Nazionale di Ripresa e Resilienza funded by the Italian Ministry of University and Research (MUR), in the framework of the European Union—NextGenerationEU—Mission 4 "Education and Research", PRIN 2022 PNRR SILCO (P2022SZANL-CUP D53D23018550001) Project.

Open access publishing facilitated by Politecnico di Milano, as part of the Wiley - CRUI-CARE agreement.

Conflicts of Interest

The authors declare no conflicts of interest.

Data Availability Statement

The data that support the findings of this study are available from the corresponding author upon reasonable request.

References

1. Intergovernal Panel on Climate Change (IPCC), "Summary for Policymakers," in *Global Warming of 1.5°C* (Cambridge University Press, 2022), 1–24, https://doi.org/10.1017/9781009157940.001.

2. A. Jarvis and P. M. Forster , "Estimated Human-Induced Warming From a Linear Temperature and Atmospheric CO_2 Relationship," *Nature Geoscience* 17 (2024): 1222–1224, https://doi.org/10.1038/s41561-024-01580-5.

3. L. Fu, Z. Ren, W. Si, et al., "Research Progress on CO_2 Capture and Utilization Technology," *Journal of CO2 Utilization* 66 (2022): 102260, https://doi.org/10.1016/j.jcou.2022.102260.

4. X. Wen, Q. Min, X. Liu, et al., "Anti-Reconstruction Cu Nanowire Catalysts Enabled by SiO_2 Encapsulation for Durable Electrochemical CO_2 Reduction," *ACS Catalysis* 15 (2025): 14215–14226, https://doi.org/10.1021/acscatal.5c03539.

5. P. Melo Bravo and D. P. Debecker, "Combining CO2 Capture and Catalytic Conversion to methane," *Waste Disposal & Sustainable Energy* 1 (2019): 53–65, https://doi.org/10.1007/s42768-019-00004-0.

6. F. Raganati, F. Miccio, and P. Ammendola, "Adsorption of Carbon Dioxide for Post-Combustion Capture: A Review," *Energy & Fuels* 35 (2021): 12845–12868, https://doi.org/10.1021/acs.energyfuels.1c01618.

7. H. Zentou, M. Aliyu, M. A. Abdalla, et al., "Advancements and Challenges in Adsorption-Based Carbon Capture Technology: From Fundamentals to Deployment," *Chemical Record* 25 (2025), https://doi.org/10.1002/tcr.202400188.

8. F. L. Mohd Rasdi, R. Jeyaseelan, M. F. Taha, and M. A. A. Mohd Razip, "Optimization of CO_2 Capture Using a New Aqueous Hybrid Solvent (MDEA-[TBPA][TFA]) With a Low Heat Capacity: Integration of COSMO-RS and RSM Approaches," *Processes* 12 (2024): 2626, https://doi.org/10.3390/pr12122626.

9. M. R. Dave, F. Vega, and N. Mahinpey, "Improvement of the Spray Column Performance for CO_2 Capture in an Amine Absorption Process Using Multiple Nozzle Arrangement," *Industrial & Engineering Chemistry Research* 63 (2024): 21519–21538, https://doi.org/10.1021/acs.iecr.4c02615.

10. D.-I. Kwon, J.-C. Kim, H. Lee, W. Lee, and C. Jo, "Engineering Micropore Walls of Beta Zeolites by Post-Functionalization for CO2 Adsorption Performance Screening Under Humid Conditions," *Chemical Engineering Journal* 427 (2022): 131461, https://doi.org/10.1016/j.cej.2021.131461.

11. M. Ilkaeva, R. Vieira, J. M. P. Pereira, M. Sardo, I. Marin-Montesinos, and L. Mafra, "Assessing CO_2 Capture in Porous Sorbents via Solid-State NMR-Assisted Adsorption Techniques," *Journal of the American Chemical Society* 145 (2023): 8764–8769, https://doi.org/10.1021/jacs.3c00281.

12. R. W. Baker, B. Freeman, J. Kniep, Y. I. Huang, and T. C. Merkel, "CO_2 Capture From Cement Plants and Steel Mills Using Membranes," *Industrial & Engineering Chemistry Research* (2018), https://doi.org/10.1021/acs.iecr.8b02574.

13. F. Ito and H. Yamada, "Effect of Process Conditions on CO_2 Permeance and Selectivity of Polyvinyl Alcohol/Sodium Polyacrylate membrane," *Polymer-Plastics Technology and Materials* 63 (2024): 1319–1328, https://doi.org/10.1080/25740881.2024.2329971.

14. A. Porta, C. Larghi, L. Lietti, and C. G. Visconti, "Once-Through CO_2 Hydrogenation to Grid-Compatible Synthetic Natural Gas Over a Ru-Based Catalyst at Atmospheric Pressure," *Catalysis Today* 442 (2024): 114907, https://doi.org/10.1016/J.CATTOD.2024.114907.

15. E. Moioli, R. Mutschler, and A. Züttel, "Renewable Energy Storage via CO_2 and H_2 Conversion to Methane and Methanol: Assessment for Small Scale Applications," *Renewable and Sustainable Energy Reviews* 107 (2019): 497–506, https://doi.org/10.1016/j.rser.2019.03.022.

16. B. Rolandi, M. Piacentini, R. Ometto, A. Porta, and C. G. Visconti, "On the Performances of Highly Promoted Fe-Zn-Cu-K Catalysts for CO2 Fischer-Tropsch Synthesis," *Applied Catalysis A: General* 708 (2025): 120590, https://doi.org/10.1016/j.apcata.2025.120590.

17. S. Molina-Ramírez, D. Peltzer, M. Cortés-Reyes, et al., "CO_2-SR Technology Using NiBa Unsupported Catalyst. Isotopic Study of Cyclic Process of CO_2 Storage and in Situ Regeneration With CH4," *Fuel* 341 (2023): 127690, https://doi.org/10.1016/j.fuel.2023.127690.

18. P. Frontera, A. Macario, M. Ferraro, and P. Antonucci, "Supported Catalysts for CO_2 Methanation: A Review," *Catalysts* 7 (2017): 59, https://doi.org/10.3390/catal7020059.

19. M. S. Duyar, M. A. A. Treviño, and R. J. Farrauto, "Dual Function Materials for CO_2 Capture and Conversion Using Renewable H_2," *Applied Catalysis B: Environmental* 168-169 (2015): 370–376, https://doi.org/10.1016/j.apcatb.2014.12.025.

20. A. Porta, R. Matarrese, C. G. Visconti, L. Castoldi, and L. Lietti, "Storage Material Effects on the Performance of Ru-Based CO_2 Capture and Methanation Dual Functioning Materials," *Industrial & Engineering Chemistry Research* 60 (2021): 6706–6718, https://doi.org/10.1021/acs.iecr.0c05898.

21. S. Cimino, F. Boccia, and L. Lisi, "Effect of Alkali Promoters (Li, Na, K) on the Performance of Ru/Al_2O_3 Catalysts for CO_2 Capture and Hydrogenation to Methane," *Journal of CO2 Utilization* 37 (2020): 195–203, https://doi.org/10.1016/j.jcou.2019.12.010.

22. A. Bermejo-López, B. Pereda-Ayo, J. A. Onrubia-Calvo, J. A. González-Marcos, and J. R. González-Velasco, "Tuning Basicity of Dual Function Materials Widens Operation Temperature Window for Efficient CO2 Adsorption and Hydrogenation to CH_4," *Journal of CO2 Utilization* 58 (2022): 101922, https://doi.org/10.1016/J.JCOU.2022.101922.

23. S. Essounani-Mérida, S. Molina-Ramírez, M. Cortés-Reyes, C. Herrera, M. Á. N. Larrubia, and L. J. Alemany, "Influence of Second Metal Incorporation on Nickel-Based Unsupported Catalysts for CO_2 Reduction (CO_2-SR) Technology," *Results in Engineering* (2025), 104921, https://doi.org/10.1016/j.rineng.2025.104921.

24. C. Jeong-Potter, A. Zangiabadi, and R. Farrauto, "Extended Aging of Ru-Ni, Na_2O/Al_2O_3 Dual Function Materials (DFM) for Combined Capture and Subsequent Catalytic Methanation of CO2 From Power Plant Flue Gas," *Fuel* 328 (2022): 125283, https://doi.org/10.1016/j.fuel.2022.125283.

25. M. A. Arellano-Treviño, Z. He, M. C. Libby, and R. J. Farrauto, "Catalysts and Adsorbents for CO_2 Capture and Conversion With Dual Function Materials: Limitations of Ni-containing DFMs for Flue Gas applications," *Journal of CO2 Utilization* 31 (2019): 143–151, https://doi.org/10.1016/J.JCOU.2019.03.009.

26. M. S. Duyar, S. Wang, M. A. Arellano-Treviño, and R. J. Farrauto, "CO 2 Utilization With a Novel Dual Function Material (DFM) for Capture and Catalytic Conversion to Synthetic Natural Gas: An update," *Journal of CO2 Utilization* 15 (2016): 65–71, https://doi.org/10.1016/j.jcou.2016.05.003.

27. C. Jeong-Potter, M. A. Arellano-Treviño, W. W. McNeary, A. J. Hill, D. A. Ruddy, and A. T. To, "Modified Cu–Zn–Al Mixed Oxide Dual Function Materials Enable Reactive Carbon Capture to Methanol," *EES Catalysis* 2 (2024), https://doi.org/10.1039/D3EY00254C.

28. S. Molina-Ramírez, M. Cortés-Reyes, C. Herrera, M. A. Larrubia, and L. J. Alemany, "CO_2-SR Cyclic Technology: CO_2 Storage and In Situ Regeneration With CH_4 Over a New Dual Function NiBa Unsupported catalyst," *Journal of CO2 Utilization* 40 (2020): 101201, https://doi.org/10.1016/j.jcou.2020.101201.

29. S. Sun, C. Zhang, S. Guan, S. Xu, P. T. Williams, and C. Wu, "Ni/Support-CaO Bifunctional Combined Materials for Integrated CO2 Capture and Reverse Water-gas Shift Reaction: Influence of Different Supports," *Separation and Purification Technology* 298 (2022): 121604, https://doi.org/10.1016/j.seppur.2022.121604.

30. G. E. de Araujo, J. H. de Castro, W. F. Monteiro, J. de Lima, R. A. Ligabue, and R. V. Lourega, "Methanation of CO_2 From Flue Gas: Experimental Study on the Impact of Pollutants," *Reaction Kinetics, Mechanisms and Catalysis* 134 (2021): 743–757, https://doi.org/10.1007/s11144-021-02092-8.

31. B. Lu, Y. Fan, X. Zhi, et al., "Material Design and Prospect of Dual-Functional Materials for Integrated Carbon Dioxide Capture and Conversion," *Carbon Capture Science & Technology* 12 (2024): 100207, https://doi.org/10.1016/j.ccst.2024.100207.

32. L.-P. Merkouri, J. L. Martín-Espejo, L. F. Bobadilla, J. A. Odriozola, M. S. Duyar, and T. R. Reina, "Flexible NiRu Systems for CO_2 Methanation: From Efficient Catalysts to Advanced Dual-Function Materials," *Nanomaterials* 13 (2023): 506, https://doi.org/10.3390/nano13030506.

33. S. Cimino, E. M. Cepollaro, and L. Lisi, "On the Effect of Li or Na Doping on Ru/TiO_2 Catalyst for CO2 Methanation," *Catalysis Today* 452 (2025): 115245, https://doi.org/10.1016/j.cattod.2025.115245.

34. S. Molina-Ramirez, G. Nava, E. Finocchio, et al., "Mesoporous Silica As A Tunable Support For Dual-Function Ba–Ru Catalysts: Impact on CO_2 Adsorption And Methanation Performance," *Microporous and Mesoporous Materials* 405 (2026): 114080, https://doi.org/10.1016/j.micromeso.2026.114080.

35. K. Karpinska-Wlizlo, W. Zawadzki, G. Slowik, and W. Gac, "Does the Active Surface Area Determine the Activity of Silica Supported Nickel Catalysts in CO_2 Methanation Reaction?," *Chemical Engineering Journal* 502 (2024): 157827, https://doi.org/10.1016/j.cej.2024.157827.

36. J. Ilsemann, M. M. Murshed, T. M. Gesing, J. Kopyscinski, and M. Bäumer, "On the Support Dependency of the CO_2 Methanation—Decoupling Size and Support Effects," *Catalysis Science & Technology* 11 (2021): 4098–4114, https://doi.org/10.1039/D1CY00399B.

37. L. Wang, Z. Wang, H. Yang, and G. Yang, "The Study of Thermal Stability of the SiO_2 Powders With High Specific Surface Area," *Materials Chemistry and Physics* 57 (1999): 260–263, https://doi.org/10.1016/S0254-0584(98)00226-0.

38. M. Milani, K. Ahmad, E. Cavalletti, et al., "Synthesis of Spherical Mesoporous Silica Beads With Tunable Size, Stiffness and Porosity," *Microporous and Mesoporous Materials* 387 (2025): 113534, https://doi.org/10.1016/j.micromeso.2025.113534.

39. Y. Shen, P. Zhao, and Q. Shao, "Porous Silica and Carbon Derived Materials From Rice Husk Pyrolysis Char," *Microporous and Mesoporous Materials* 188 (2014): 46–76, https://doi.org/10.1016/j.micromeso.2014.01.005.

40. C. Allegretti, E. Bellinetto, P. D'Arrigo, et al., "Fractionation of Raw and Parboiled Rice Husks With Deep Eutectic Solvents and Characterization of the Extracted Lignins Towards a Circular Economy Perspective,"

Molecules (Basel, Switzerland) 27 (2022): 8879, https://doi.org/10.3390/molecules27248879.

41. D. Montini, C. Cara, M. D'Arienzo, et al., "Recent Advances on Porous Siliceous Materials Derived From Waste," *Materials* 16 (2023): 5578, https://doi.org/10.3390/ma16165578.

42. R. S. Gärtner and G.-J. Witkamp, , "Mixed Solvent Reactive Recrystallization of Trona (Sodium sesqui-carbonate) Into Soda (Sodium carbonate anhydrate)," *Hydrometallurgy* 88 (2007): 75–91, https://doi.org/10.1016/j.hydromet.2007.03.006.

43. K. M. Bisson, K. A. Welch, S. A. Welch, et al., "Patterns and Processes of Salt Efflorescences in the McMurdo region, Antarctica," *Arctic, Antarctic, and Alpine Research* 47 (2015): 407–425, https://doi.org/10.1657/AAAR0014-024.

44. G. Busca , "Infrared (IR) Spectroscopy," in *Springer Handbook of Advanced Catalyst Characterization* Springer Nature (2023), 3–32.

45. L. M. F. Lopes and L. M. Ilharco, "Hydrofluoric Acid-induced Fluorination and Formation of Silica Nanocapsules for ^{19}F Magnetic Resonance Imaging," *RSC Advances* 4 (2014): 16931–16934, https://doi.org/10.1039/C3RA47842D.

46. G. Busca and V. Lorenzelli, "Infrared Spectroscopic Identification of Species Arising From Reactive Adsorption of Carbon Oxides on Metal Oxide Surfaces," *Materials Chemistry* 7 (1982): 89–126, https://doi.org/10.1016/0390-6035(82)90059-1.

47. G. Ramis, G. Busca, and V. Lorenzelli, "Low-temperature CO_2 Adsorption on Metal Oxides: Spectroscopic Characterization of Some Weakly Adsorbed Species," *Materials Chemistry and Physics* 29 (1991): 425–435, https://doi.org/10.1016/0254-0584(91)90037-U.

48. G. Busca, "Catalytic Materials Based on Silica and Alumina: Structural Features and Generation of Surface Acidity," *Progress in Materials Science* 104 (2019): 215–249, https://doi.org/10.1016/j.pmatsci.2019.04.003.

49. P. A. Kots, T. Xie, B. C. Vance, et al., "Electronic Modulation of Metal-Support Interactions Improves Polypropylene Hydrogenolysis Over Ruthenium Catalysts," *Nature Communications* 13 (2022), https://doi.org/10.1038/s41467-022-32934-5.

50. G. Garbarino, D. Bellotti, E. Finocchio, L. Magistri, and G. Busca, "Methanation of Carbon Dioxide on Ru/Al_2O_3: Catalytic Activity and Infrared Study," *Catalysis Today* 277 (2016): 21–28, https://doi.org/10.1016/j.cattod.2015.12.010.

51. S. Y. Chin, C. T. Williams, and M. D. Amiridis, "FTIR Studies of CO Adsorption on Al_2O_3 - and SiO_2 -Supported Ru Catalysts," *Journal of Physical Chemistry B* 110 (2006): 871–882, https://doi.org/10.1021/jp053908q.

52. G. Nava, A. Porta, C. G. Visconti, and R. Matarrese, "Impact of Sorbent-Catalyst Layouts on Ru/K-Based DFMs for Integrated CO2 Capture and Methanation," *Applied Catalysis A: General* 709 (2026): 120654, https://doi.org/10.1016/j.apcata.2025.120654.

53. A. Porta, R. Matarrese, C. G. Visconti, and L. Lietti, "Investigation of DFMs for CO_2 Capture and Methanation by Coupled Microreactor Experiments and FT-IR Spectroscopy," *Energy & Fuels* 37 (2023): 7280–7290, https://doi.org/10.1021/acs.energyfuels.3c00443.

54. C. J. Keturakis, F. Ni, M. Spicer, M. G. Beaver, H. S. Caram, and I. E. Wachs, "Monitoring Solid Oxide CO_2 Capture Sorbents in Action," *ChemSusChem* 7 (2014): 3459–3466, https://doi.org/10.1002/cssc.201402474.

55. G. Busca, "Spectroscopic Characterization of the Acid Properties of Metal Oxide Catalysts," *Catalysis Today* 41 (1998): 191–206, https://doi.org/10.1016/S0920-5861(98)00049-2.

56. F. Frola, M. Manzoli, F. Prinetto, G. Ghiotti, L. Castoldi, and L. Lietti, "Pt−Ba/Al_2O_3 NSR Catalysts at Different Ba Loading: Characterization of Morphological, Structural, and Surface Properties," *Journal of Physical Chemistry C* 112 (2008): 12869–12878, https://doi.org/10.1021/jp801480t.

57. F. Prinetto, M. Manzoli, S. Morandi, et al., "Pt−K/Al_2O_3 NSR Catalysts: Characterization of Morphological, Structural and Surface Properties," *Journal of Physical Chemistry C* 114 (2010): 1127–1138, https://doi.org/10.1021/jp909026p.

58. L. Proaño, E. Tello, M. A. Arellano-Trevino, S. Wang, R. J. Farrauto, and M. Cobo, "In-Situ DRIFTS Study of Two-Step CO2 Capture And Catalytic Methanation Over Ru,"Na2O"/Al2O3 Dual Functional Material," *Applied Surface Science* 479 (2019): 25–30, https://doi.org/10.1016/j.apsusc.2019.01.281.

59. C. Jeong-Potter, A. Porta, R. Matarrese, C. G. Visconti, L. Lietti, and R. Farrauto, "Aging Study of Low Ru Loading Dual Function Materials (DFM) for Combined Power Plant Effluent CO_2 Capture and Methanation," *Applied Catalysis B: Environmental* 310 (2022): 121294, https://doi.org/10.1016/j.apcatb.2022.121294.

60. S. Wang, E. T. Schrunk, H. Mahajan, and A. R. J. Farrauto, "The Role of Ruthenium in CO_2 Capture and Catalytic Conversion to Fuel by Dual Function Materials (DFM)," *Catalysts* (2017), 88, https://doi.org/10.3390/catal7030088.

61. S. Cimino, E. M. Cepollaro, M. Pazzi, and L. Lisi, "Sulphur Poisoning and Regeneration of Li-Ru/Al_2O_3 Dual Function Material for the Integrated CO_2 Capture and Methanation," *Catalysis Today* 426 (2024): 114366, https://doi.org/10.1016/j.cattod.2023.114366.

62. K. I. Hadjiivanov and G. N. Vayssilov , "Characterization of Oxide Surfaces and Zeolites by Carbon Monoxide as an IR Probe Molecule," *Advances in Catalysis* 47 (2002): 307–511.

63. X. Wang, Y. Hong, H. Shi, and J. Szanyi, "Kinetic Modeling and Transient DRIFTS–MS Studies of CO_2 Methanation Over Ru/Al_2O_3 catalysts," *Journal of Catalysis* 343 (2016): 185–195, https://doi.org/10.1016/j.jcat.2016.02.001.

64. L. Falbo, C. G. Visconti, L. Lietti, and J. Szanyi, "The Effect of CO on CO_2 Methanation Over Ru/Al_2O_3 Catalysts: A Combined Steady-State Reactivity and Transient DRIFT Spectroscopy Study," *Applied Catalysis B: Environmental* 256 (2019): 117791, https://doi.org/10.1016/j.apcatb.2019.117791.

65. L. Proaño, M. A. Arellano-Treviño, R. J. Farrauto, M. Figueredo, C. Jeong-Potter, and M. Cobo, "Mechanistic Assessment Of Dual Function Materials, Composed Of Ru-Ni, Na_2O/Al_2O_3 and Pt-Ni, Na_2O/Al_2O_3, for CO_2 Capture And Methanation By In-Situ DRIFTS," *Applied Surface Science* 533 (2020): 147469, https://doi.org/10.1016/j.apsusc.2020.147469.

66. M. Kantcheva and S. Sayan, "On the Mechanism of CO Adsorption on a Silica-Supported Ruthenium Catalyst," *Catalysis Letters* 60 (1999): 27–38, https://doi.org/10.1023/A:1019082218590.

67. S. Bahrami Gharamaleki, S. Carrasco Ruiz, T. Ramirez Reina, M. Short, and M. S. Duyar, "Effect of Adsorbent Loading On NaNiRu-DFMs' CO_2 Capture And Methanation: Finding Optimal Na-Loading Using Bayesian Optimisation Guided Experiments," *Industrial Chemistry & Materials* 4 (2026): 78–92, https://doi.org/10.1039/D5IM00019J.

68. J. Gao, Y. Wang, Y. Ping, et al., "A Thermodynamic Analysis of Methanation Reactions of Carbon Oxides for the Production of Synthetic Natural Gas," *RSC Advances* (2012), https://doi.org/10.1039/c2ra00632d.

69. T. Oliveira Cabral, F. Bellot Noronha, and F. Souza Toniolo, "Kinetic and DRIFTS Studies of the CO_2 Catalytic Hydrogenation on Ru/SiO2: A Comprehensive and Strategic Investigation of CO_2 Methanation Mechanisms by Kinetic Modeling and Data Regression," *Chemical Engineering Journal* 485 (2024): 149716, https://doi.org/10.1016/j.cej.2024.149716.

70. S. Deng, C. Zhu, X. Fang, X. Xu, and X. Wang, "Lithium Cation Modification Markedly Enhances Ru Dispersion and CO_2 Methanation Activity on Ru/SiO_2 Catalysts," *ACS Catalysis* 15 (2025): 7666–7676, https://doi.org/10.1021/acscatal.5c00176.

71. I.-G. Bajusz and J. G. Jr. Goodwin, "Hydrogen and Temperature Effects on the Coverages and Activities of Surface Intermediates During Methanation on Ru/SiO_2," *Journal of Catalysis* 169 (1997): 157–165, https://doi.org/10.1006/jcat.1997.1695.

72. A. Porta, C. G. Visconti, L. Castoldi, et al., "Ru-Ba Synergistic Effect in Dual Functioning Materials for Cyclic CO_2 Capture and Methanation,"

Applied Catalysis B: Environmental 283 (2021): 119654, https://doi.org/10.1016/J.APCATB.2020.119654.

73. S. Sapru, K. D. Hart, C. Zhou, et al., "Long-Range Metal–Sorbent Interactions Determine CO_2 Capture and Conversion in Dual-Function Materials," *ACS Nano* 19 (2025): 2484–2496, https://doi.org/10.1021/acsnano.4c13606.

74. J. A. Martins, V. F. D. Martins, C. V. Miguel, A. E. Rodrigues, and L. M. Madeira, "A Cyclic Sorption-Reaction Process for Continuous Synthetic Methane Production From Flue Gas and Green Hydrogen," *Chemical Engineering Journal* 476 (2023): 146375, https://doi.org/10.1016/j.cej.2023.146375.

75. D. Liu, L. Chen, X. Zhu, J. Ma, and K. Liu, "Spatial Arrangements of Dual Functional Materials for CO_2 Capture and In-Situ Methanation at Low Temperature," *Chemical Engineering Journal* 511 (2025): 162186, https://doi.org/10.1016/j.cej.2025.162186.

76. K. Mori, A. Fujimoto, K. Shun, H. Yamashita, S. Ishikawa, and K. Motokura, "Insight Into Interparticle Hydrogen Spillover Driven by Remote Metal Oxides," *ACS Applied Materials & Interfaces* 17 (2025): 43926–43935, https://doi.org/10.1021/acsami.5c10678.

Supporting Information

Additional supporting information can be found online in the Supporting Information section.

Supporting File: cctc70669-sup-0001-SuppMat.docx.